

Ultrasmall Mode Volume Hyperbolic Nanocavities for Enhanced Light–Matter Interaction at the Nanoscale

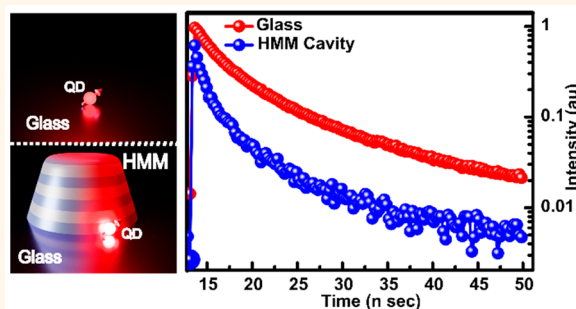
S. R. K. Chaitanya Indukuri,[‡] Jonathan Bar-David,[‡] Noa Mazurski, and Uriel Levy^{*†}

Department of Applied Physics, Faculty of Science and the Center for Nanoscience and Nanotechnology, The Hebrew University of Jerusalem, Jerusalem, 91904, Israel

Supporting Information

ABSTRACT: Cavities are the building blocks for multiple photonic applications from linear to nonlinear optics and from classical optics to quantum electrodynamics. Hyperbolic metamaterial cavities are one class of optical cavities that have recently been realized and shown to possess desirable characteristics such as engineered refractive indices and ultrasmall mode volumes, both beneficial for enhancement of light–matter interactions at the nanoscale. We hereby report the design, fabrication, and experimental characterization of nanoscale hyperbolic metamaterial cavities at the visible frequency. We show experimentally that these nanocavities enhance the light–matter interaction at the nanoscale and demonstrate increased photonic density of states and enhanced free space radiation efficiency of quantum dots coupled to such cavities, thus demonstrating the importance of hyperbolic metamaterial cavities for applications in solid-state light sources, quantum technologies, and cavity quantum electrodynamics.

KEYWORDS: hyperbolic nanocavities, quantum dots, Purcell factor, light–matter interaction, far-field radiation enhancement, nanoscale cavity quantum electrodynamics



In the fields of quantum information processing and quantum communications it is highly desirable to engineer optical nanocavities with ultrasmall mode volumes (V_m) that can be strongly coupled to quantum emitters for the purpose of enhancing light–matter interaction.^{1–5} Examples include most dielectric microcavities such as microspheres,⁶ microdisks,⁷ and photonic crystals⁸ designed to enhance the light–matter interaction. In such cavities, high quality factors (Q-factor) can be achieved alongside with mode volumes on the order of a wavelength.⁹ The strong light–matter interaction in and around these cavities is useful for different applications in nanophotonics including nonlinear optics,¹⁰ optomechanics,¹¹ and quantum optics.¹² However, further reduction in cavity sizes and mode volumes of dielectric cavities is limited by the dielectric constant of the cavity materials and by the index contrast between the cavity and surrounding medium, resulting in deterioration of the Q-factor for reduced cavity size,¹³ which sets a restriction for true nanoscale manipulation of light.

Alternatively, in metallic nanostructures, electromagnetic fields are confined within the cavity due to the properties of the metal, including the capability to support surface plasmon polariton (SPP) modes on the metal–dielectric interface. This evanescent confinement is due to the SPP dispersion.¹⁴ These

confined modes create strong field enhancement and can be used for creating cavities with ultrasmall mode volumes.¹⁵ Plasmonic nanocavities have been proposed theoretically as a means to create ultrasmall modal volumes, whereas experimental demonstrations push cavity sizes down to $(\lambda/3)^3$.¹⁶ Very recently, plasmonic nanocavity patch antennas were used for enhancing fluorescent emission,^{17–19} lasing,²⁰ and even strong coupling of a single molecule to a cavity mode.²¹ However, drawbacks of metallic or plasmonic cavities include the random cavity formation on the sample surface and sometimes incompatibility with modern nanofabrication techniques. Therefore, the search for nanocavities with ultrasmall mode volume and high refractive index for enhancement of light–matter interaction and as a platform for cavity-quantum electrodynamics (QED) applications continues.

In parallel, artificial nanostructures designed to manipulate light at the nanoscale are known as metamaterials,²² which are engineered nanostructure with artificial optical properties. The

Received: July 22, 2019

Accepted: October 7, 2019

Published: October 7, 2019

use of metamaterials' optical characteristics such as negative or zero refractive index,²³ artificial birefringence and dichroism, and engineered dispersion has enabled the demonstration of super-resolution imaging,²⁴ cloaking,^{25,26} and ultrahigh refractive index.²⁷ Recently, the effect of nonlocality on the Purcell's factor of a quantum emitter inside metamaterials was demonstrated.²⁸

A subclass of metamaterials is that of hyperbolic metamaterials, which show the optical equivalent of a "Lifshitz transition", also known as optical topological transitions.^{29,30} Typical hyperbolic metamaterials (HMMs) are indefinite media made of thin, alternating layers of metallic and dielectric materials, in a manner creating strong birefringence and resulting in a hyperbolic dispersion surface in momentum space, contrary to the ellipsoidal or spherical dispersion of natural materials, as shown schematically in Figure 1(a,b). This

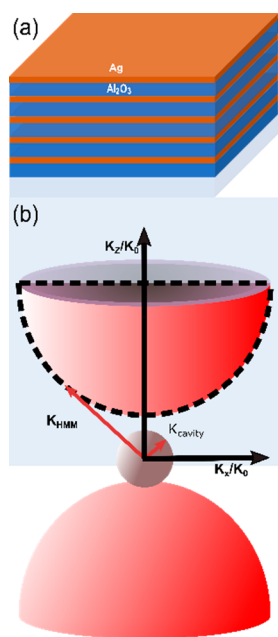


Figure 1. (a) Schematic diagram of the hyperbolic structure containing multilayers of dielectric (Al_2O_3) and metal (Ag) layers. (b) Schematic diagram of the hyperbolic isofrequency surface for multilayer hyperbolic metamaterials which includes the spherical isofrequency surface of free space.

hyperbolic dispersion leads to dramatic changes in the photonic local density of states (LDOS) in and around the metamaterial.^{30–35} The changes in the LDOS result in broadband enhancement of the emission of quantum emitters (QEs) inside and on top of bulk HMMs,³⁶ with a theoretical Purcell factor of up to $(\lambda/a)^3$ (where a is a lattice constant of multilayers) in such systems.^{37,38} Experimentally, the Purcell factor enhancement near HMMs was shown to reach values of 10^2 – 10^4 for quantum emitters placed inside the HMM.^{36,39} Previous reports were concentrated on the coupling of QEs to bulk HMM modes, which eventually converts into heat due to ohmic losses in the metal layers embedded in the HMM.⁴⁰ Even though such coupling enhances the decay rate of the quantum emitters, the far-field radiation is not enhanced due to lack of an efficient out-coupling mechanism.^{41,42} Therefore, in order to enhance the free-space radiation efficiency of quantum emitters and light-emitting devices, the free-space coupling must be addressed, as lifetime shortening alone is

insufficient. This is of significance for applications of quantum communications as well as solid-state light-emitting devices. In this context, enhanced free-space emission was shown in an HMM grating structure,^{43,44} but these grating structures still limit the use in nanoscale optical devices.

In this paper, we demonstrate far-field radiation enhancement and lifetime shortening of quantum emitters by coupling to subwavelength HMM nanocavities with engineered resonant optical frequencies. HMM cavities were theoretically proposed by Jie Yao *et al.*⁴⁵ and realized by Xiodong Yang *et al.*,⁴⁶ at near-infrared frequencies. These cavities have been shown to yield an anomalous scaling law causing cavities of different sizes to have the same resonance frequency. A theoretical prediction of free-space radiative enhancement was calculated to be up to 100-fold for a dipole in great proximity to the cavity.^{47,48}

However, to date there is no experimental demonstration of coupling between HMM cavities and quantum emitters at visible frequencies. Specifically, previous demonstrations lack the spectral overlap between cavity eigenmodes and quantum dots' emission spectrum, and therefore free-space radiative emission enhancement (FREE) of quantum emitters coupled to HMM cavities was not demonstrated.

Below we discuss the design of HMM cavities engineered for FREE and experimentally demonstrate the lifetime shortening and emission enhancement of quantum dots placed around such structures.

Figure 1(a) shows the alternating metal–dielectric multilayer stack, which is one example of hyperbolic metamaterials.⁴⁹ The thickness of the metals and dielectrics are t_m and t_d , respectively, and therefore the metal filling fraction is defined as $f = \frac{t_m}{t_m + t_d}$. Both metal and dielectric layers are of subwavelength thickness ($t_m, t_d \ll \lambda$), which allows us to approximate this multilayer system as a uniform effective medium whose dielectric tensor can be calculated using the Maxwell–Garnet effective medium theory. Figure 1(b) shows the schematic diagram of the hyperbolic isofrequency topology of our HMM medium, compared to the circular isofrequency topology for light propagation in the isotropic medium.

The effective refractive index of a cavity is defined as $n_{\text{eff}} = K_{\text{cavity}}/K_0$, where K_{cavity} is the wave vector in the cavity and K_0 is the free-space wave vector. The fundamental bottleneck to reduce mode volume in dielectric cavities below the subwavelength limit is the limited dielectric constant of dielectric materials used to form the cavities. This fundamental limit can be described by the closed spherical isofrequency surface of these dielectrics. As the mode volume of the dielectric cavity keeps decreasing to reach the order of the wavelength, the wavevector inside the cavity increases and reaches the radius of the isofrequency surface. Further reduction of the cavity size requires the wavevector to be larger than the radius of the isofrequency surface. As a result, no propagating modes are allowed. These large wavevectors are evanescent.

In contrast, for the case of ideal hyperbolic metamaterials, the cavity wavevector K_{HMM} may have infinite values at any frequency, due to the engineered refractive index. Therefore, one can achieve any cavity wavevector (propagating) and effective refractive index $n_{\text{effective}}$ with allowed K_{HMM} values, and thus the cavities can be realized in true subwavelength dimensions. Due to the scaling of $n_{\text{effective}}$ with K_{HMM} , different hyperbolic cavities share the same resonant frequency if they

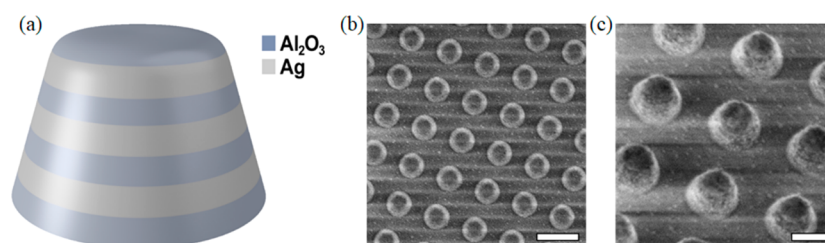


Figure 2. (a) Schematic diagram of the cavity with tilted side walls. (b) FESEM image of the cavity array size of 105 nm (scale bar 500 nm). (c) FE-SEM image of the single cavity (scale bar 200 nm).

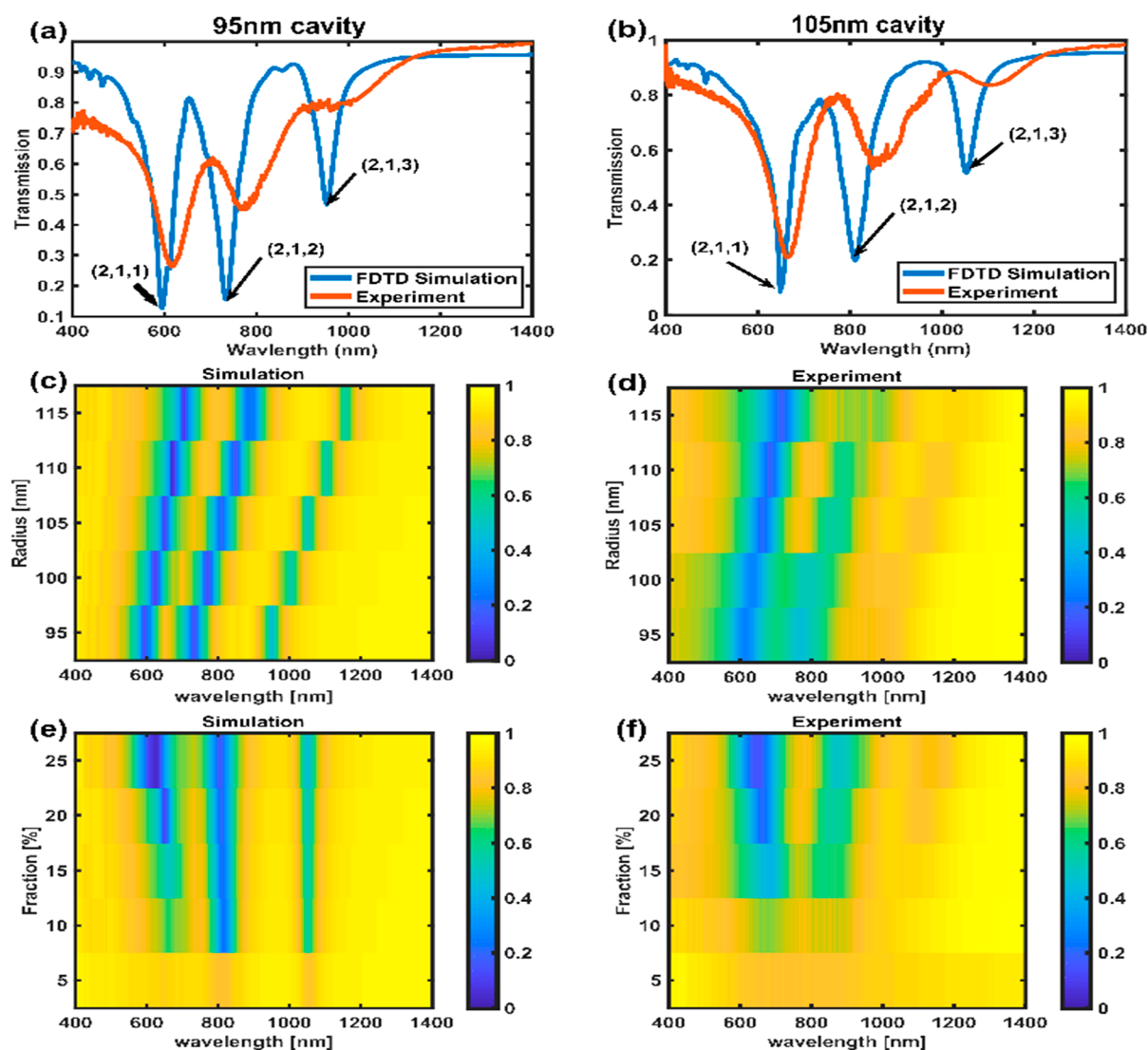


Figure 3. (a, b) Experimental results and FDTD simulations of the transmission spectrum from cavity arrays with a radius of 95 nm (a) and 105 nm (b). (c, d) Color map showing the simulated and measured transmission as a function of wavelength and cavity radius. (e, f) Color map showing the simulated and measured transmission as a function of wavelength and cavity filling fraction.

reside at the same hyperbolic isofrequency topological surface. The allowed K_{HMM} values of practical multilayer metamaterials are only restricted by the material losses and effective thickness of the multilayers. The black dotted line in Figure 1(b) shows the XZ cut of the hyperbolic isofrequency topology.

RESULTS AND DISCUSSION

To enable the enhancement of solid-state light-emitting devices, we have fabricated the designed circular nanoscale

HMM cavities having different radii from 95 to 115 nm, with a constant height of 125 nm. Our HMM structure consists of alternating metallic (Ag, silver) and dielectric layers (Al_2O_3 , alumina) with a thickness of 16 and 24 nm, respectively, schematically depicted in Figure 2(a). The thickness of each layer and the periodicity are very small compared to the wavelength of light. This small period allows us to model an effective dielectric constant of a multilayer using effective medium theory (EMT). Our device consists of three such

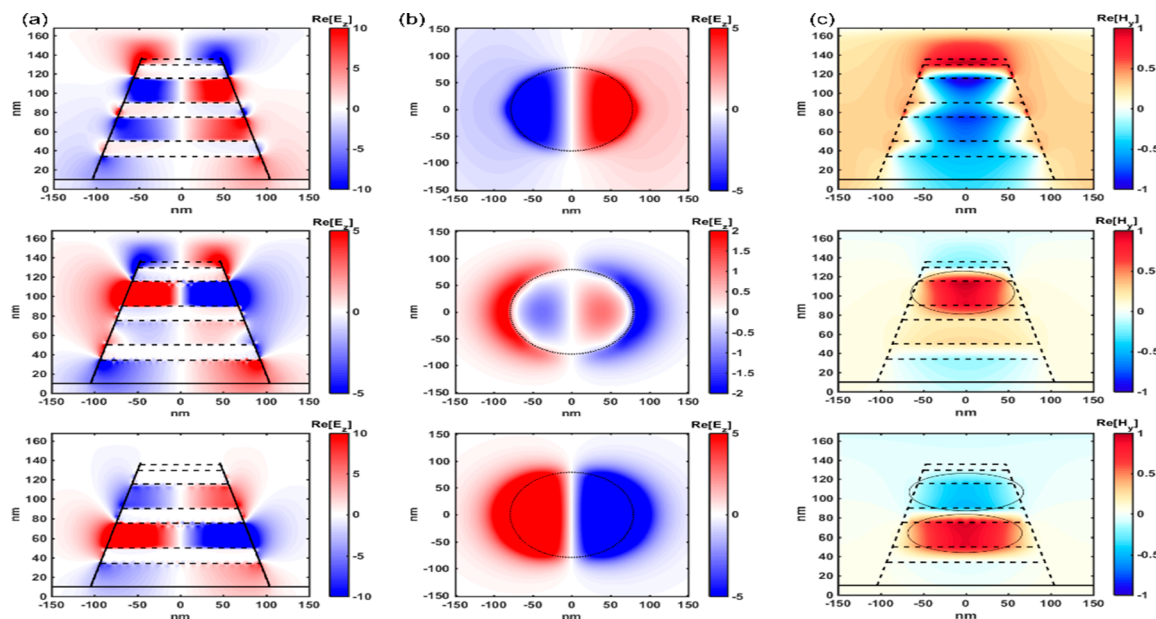


Figure 4. (a) Electric field profile of the cavity resonance for the 105 nm cavity radius at three different resonant modes. Electric field profile at 648, 810, and 1053 nm corresponding to modes (2,1,1), (2,1,2), and (2,1,3), respectively. (b) Electric field profile of the cavity resonance for a 105 nm cavity radius at three different resonant modes. Electric field profile at 648, 810, and 1053 nm corresponding to modes (2,1,1), (2,1,2), and (2,1,3), respectively.

periods and a 5 nm dielectric spacer layer on top of the cavity; thus the total thickness is 125 nm. Figure 2(b) shows a scanning electron microscope (SEM) image of one of our cavity arrays, with a cavity radius of 105 nm, made by nanofabrication techniques (see Methods). From the figure, it is clear that the side walls of the cavity are inclined. This is due to the lift-off process used in the nanofabrication. The inclination angle was assessed to be $\sim 65^\circ$ by high-resolution SEM images. Figure 2(c) shows the high-resolution image of the same array.

As mentioned earlier, the effective dielectric components of the dielectric tensor of these metal–dielectric multilayer metamaterials are calculated by EMT. The dielectric constant of Al_2O_3 is taken as 2.56, and for silver the Drude model is used, with a metal filling fraction of 0.4.³¹ More details on these effective medium calculations are given in the Supporting Information. From the effective medium calculations, we see that for wavelengths longer than 500 nm one of the principal components of the dielectric tensor becomes negative. Therefore, beyond this wavelength, the topology of our structure’s isofrequency surface becomes hyperbolic. The transitions from spherical topology to a hyperbolic topology of an isofrequency surface is known as a “topological transition”, and beyond this transition point our cavities behave as a type II hyperbolic metamaterial.

Before we use these hyperbolic nanocavities for enhancing light–matter interactions, it is important to show that these nanocavities indeed support type II hyperbolic dispersion. To do so, we have experimentally measured the transmission of these cavity arrays and compared these measurements to a numerically calculated transmission spectrum using 3D finite difference time domain (FDTD) simulations. Figure 3 shows the experimentally measured transmission alongside the numerically calculated values. Figure 3(a) shows the transmission spectrum and matching simulations of two circular cavities with radii of 95 and 105 nm, respectively, with the area fraction being 20% for both arrays. Experimental results are in

good agreement with the spectra obtained from the FDTD simulation. In the FDTD simulation, we have taken into account an inclination angle of 65° . Both measured and simulated transmission results show three dips corresponding to three different resonant modes of the cavity. These three modes are identified as modes (2,1,1), (2,1,2), and (2,1,3), respectively, as shown in Figure 3(a,b). The mode indices are numbered according to the number of half-wavelengths in the standing wave behavior of the electric field along the z -axis (E_z) inside the cavities.^{46,50} The resonant modes’ signatures in our transmission measurements are broadened and of lower contrast relative to the simulation, due to the limited coupling strength between the cavities and incident plane wave and fabrication imperfections (such as roughness and cavity size distribution). The small red-shift of the cavity resonance is probably due to a small deviation from the expected side-wall tilt from the simulated 65° .

Figure 3(c,d) show a 2D color map of the transmission as a function of wavelength and cavity radius. Five different cavity sizes were considered in both simulation and experiment, respectively, as indicated in the figure. All three modes have the same type of spectral tuning with the cavity size but with different spectral positions. Figure 3(e,f) show a 2D color map of the transmission as a function of wavelength and cavity area filling fraction. The cavity radius was fixed at 105 nm. For changing the area fraction of the cavities, we have changed the lattice spacing between the cavities in both the simulation and experiment. For the least filling fraction of 5% we are not able to observe the three-cavity resonance; rather we observed the broad dip in the transmission spectrum overlapping all three modes (see Supporting Information). This is due to the very small coupling efficiency of cavities in sparse arrays. By increasing the area fraction we begin to observe all three modes with increased coupling strength. All the individual plots for transmission shown in Figure 3(c,d) and (e,f) are provided in the Supporting Information.

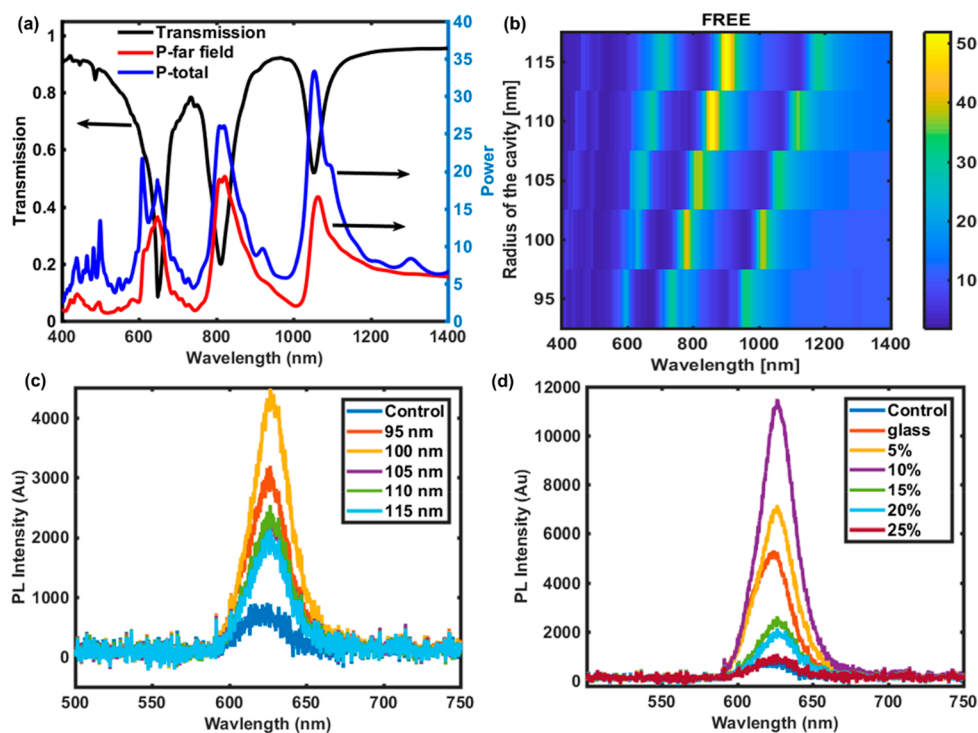


Figure 5. (a) FDTD simulation showing the enhancement of both the power radiated to the far-field and the total power emitted by the broadband quantum dot which is the proximity of the cavity size 105 nm (see Supporting Information for more details). The figure also shows the simulated transmission spectrum for the same cavity (b) color map showing the far-field radiation power enhancement (FREE) as a function of cavity size and wavelength. (c) Measured far-field emission from the QD coupled to HMM cavities with different cavity size. (d) Measured far-field emission from the QD coupled to HMM cavities with a different filling fraction. The slight asymmetry in the PL emission spectrum from the bare glass sample is probably the result of surface states. All calculation is for a dipole positioned 4 nm away from the cavity base (see Figure S13) and polarized along the z -axis.

To better understand the physical nature of our cavities' resonant modes, we have plotted some of the E_z and H_y electromagnetic field components for an HMM cavity with a radius of 105 nm and a filling fraction of 20%. Figure 4 (column a) shows a cross-section of the E_z component in the xz plane for the (2,1,1) mode at $\lambda = 648$ nm (top panel), (2,1,2) mode at $\lambda = 810$ nm (center panel), and (2,1,3) mode at $\lambda = 1053$ nm (bottom panel). Figure 4 (column b) shows cross-sections of the E_z component in the xy plane (in the same order), while Figure 4 (column c) shows a cross-section of the H_y component, again in the xz plane. The (2,1,1) and (2,1,2) modes have strong dipolar fields in the x -direction (see Supporting Information) and are therefore strong scattering modes for illumination in the z -direction, as is seen in our experimental results presented in Figure 3. By reciprocity, these modes should also be efficient couplers of the near-field to radiation. As seen in Figure 4 (columns a and b, top and center panels), these modes have higher order multipole moments of the E_z component along the z -axis, which provides a large k -vector suitable for excitation of quantum emitters.

The difference between the (2,1,1) and the (2,1,2) modes lies in the behavior of the internal fields: the (2,1,1) is a "plasmon-like" mode with a near-zero E_x internal field (*i.e.*, the field is weak within the material), whereas the (2,1,2) mode is of "dielectric-like" nature with a strong internal dipolar field. As a result, the (2,1,1) has a stronger dipole moment seen as a stronger scattering in our experiments (see Figure 3).

The (2,1,3) mode at $\lambda = 1053$ nm is a high-order multipolar mode with a weak dipole moment ("dark" mode, see Supporting Information) and therefore does not couple well

to radiation (although in principle it may couple strongly to localized sources due to its high k -vector). This behavior may be seen in our experimental results presented in Figure 3, where the (2,1,3) mode is poorly interacting with radiation.^{51,52} It should be stated that the (2,1,2) and (2,1,3) modes are similar to the modes seen in bulk hyperbolic materials with type II dispersion.^{53–56} Due to the strong dipole moment of the (2,1,1) mode, it is particularly suitable for near-field coupling to quantum emitters such as quantum dots located outside the cavity. In the case of quantum dots placed inside the cavity, the (2,1,2) and (2,1,3) are more relevant.

It is worth discussing here the physical nature of the high-wavenumber modes in our nanocavities, which are depicted in Figure 4. In the case of infinite bulk multilayer hyperbolic metamaterials, the high-wavevector modes arise from the coupling of SPPs at the interfaces of the dielectric layer with the surrounding metal. Such coupled modes are known as Bloch or volume plasmon polaritons.⁵⁷ When the bulk multilayer stack is patterned and nanocavities of metal–dielectric multilayers are generated, these Bloch or volume plasmon polaritons form standing waves inside the cavity due to large momentum mismatch between the cavity and surrounding medium (air), which results in boundary reflection in the transverse direction. For cylindrical nanocavities, these modes are called Hankel-type SPPs, as they are described mathematically by Hankel functions.^{58,59}

After characterizing our HMM cavities, we have studied whether these structures may enhance the far-field radiation of quantum dots, a question previously studied theoretically but not experimentally, for our structure.⁴⁷

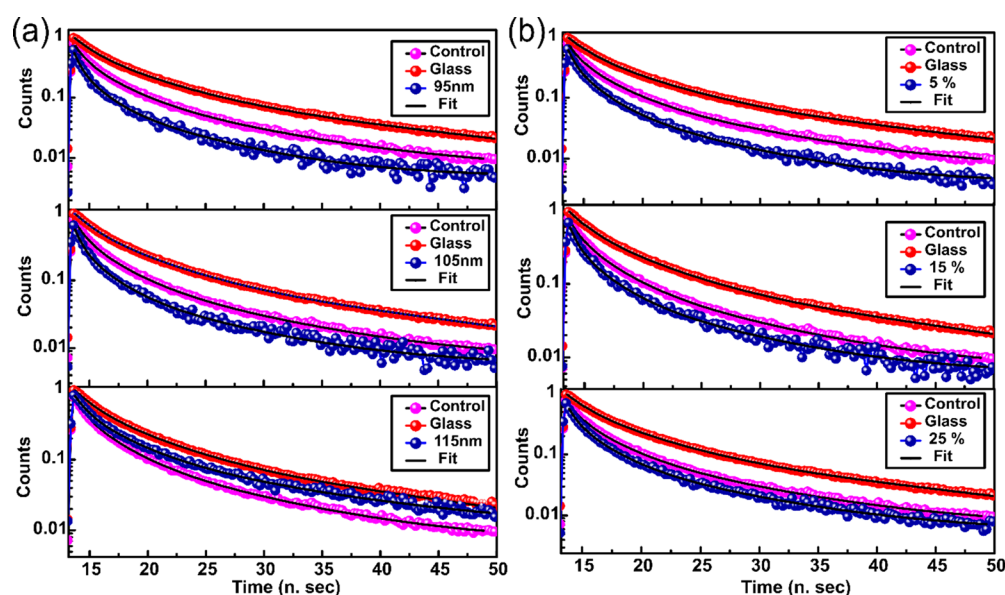


Figure 6. (a) Time-resolved decay curves as a function of three different sized cavities. (b) Time-resolved decay curves as a function of three different cavity filling fractions for a 105 nm cavity radius.

Most of the previous experiments on quantum emitters coupled to hyperbolic metamaterials demonstrated total decay rate enhancement due to large LDOS. The total decay rate is proportional to Purcell's factor of the quantum emitter in the HMM environment. This Purcell's enhancement includes not only enhancement of radiative modes but also the emission to the nonradiative modes in the HMM which may not couple to the far field due to metal losses.⁶⁰ To increase far-field emission enhancement, the device should provide a high scattering rate as compared to the rate of absorption. In our experiment we have demonstrated enhanced far-field emission, also called enhanced useful radiation (EUR).⁶¹ This figure of merit seems to fit better to applications where the radiative emission rate is of interest. Figure 5(a) shows the normalized far-field power radiation rate enhancement as a function of wavelength for a broadband dipole source in the proximity of our HMM cavity. In Figure 5(a), we have also shown the simulated transmission spectrum of the same cavity for comparison. Far-field radiation emission enhancement rate (FREE) calculated using power radiated to the far-field and details of these calculations are given in the Supporting Information. From Figure 5(a), it is clear that FREE has a peak at the wavelength corresponding to the cavity modes. This indicates the significance of cavity resonance in FREE processes. Figure 5(c) shows the FREE map for different cavities as a function of wavelength. This figure is very similar to Figure 3(b) and indicates that for all cavities FREE matches with their corresponding resonance mode.

To experimentally demonstrate this far-field emission enhancement, we performed steady-state PL measurements on a monolayer QD coupled to an HMM cavity array. The density of QDs was carefully controlled to obtain a uniform QD density around all the cavities. Figure 5(b) shows the measured PL emission enhancement from cavities with different sizes as compared to the control sample. The control sample consists of a very large multilayer pad ($200\ \mu\text{m} \times 200\ \mu\text{m}$), and the beam size in the experiment is on the order of $5\ \mu\text{m}$. For all practical purposes, we can consider the control sample as bulk HMM.

All HMM cavity sizes show enhancement compared to the control sample. The far-field emission shows nonmonotonic variation with cavity size. This is due to the change in the spectral overlap between cavity resonance and QD emission spectrum for different cavity sizes, this being a typical nanoantenna behavior. The maximal emission enhancement is obtained for cavities with a radius of 100 nm, which indicates that this is the cavity structure having the best spectral overlap between the cavity resonance and the QD's emission spectrum.

Figure 5(d) shows the PL spectra of cavities with a radius of 105 nm for cavity arrays having different filling fraction (*i.e.*, varying periodicity). One can note two important results: (a) the photoluminescence (PL) of QDs deposited on the HMM structures (both bulk and cavities) is red-shifted compared to the PL of QDs on glass. This red-shift is weakly dependent on the cavity size and is attributed to the effect of spectral variation of the Purcell factor over the QD emission spectrum.⁶² (b) We see emission enhancement (compared to bulk HMM) for all cavity periodicities. At small filling fraction (5% and 10%), the PL is enhanced also relative to the PL of QDs on the glass (~ 1.2 for 5% and ~ 1.68 for 10% filling fraction as compared with PL emission from the bare glass substrate; for simplicity of calculation, the enhancement is defined as the ratio between peak intensity in the PL spectrum of QDs coupled to the HMM cavity and glass, respectively). This is an important result, as it shows beyond doubt that the far-field emission that is enhanced by HMM cavities dominates over the lossy decay channels in both HMM cavity (5% and 10%) materials. Therefore, properly designed HMM cavities can be used for the purpose of far-field radiation emission enhancement in solid-state light-emitting devices. As the filling fraction of the cavities increases, the enhancement decreases due to quenching, and at a filling fraction of $\sim 25\%$ the emission intensity reaches that of the control sample (bulk hyperbolic metamaterial, *i.e.*, filling fraction of 100%).

To demonstrate the increase in radiation rate from the QDs, we have also performed time-resolved measurements on a QD monolayer placed on top of the cavity arrays. Figure 6 shows the time-resolved photoluminescence measurements from a

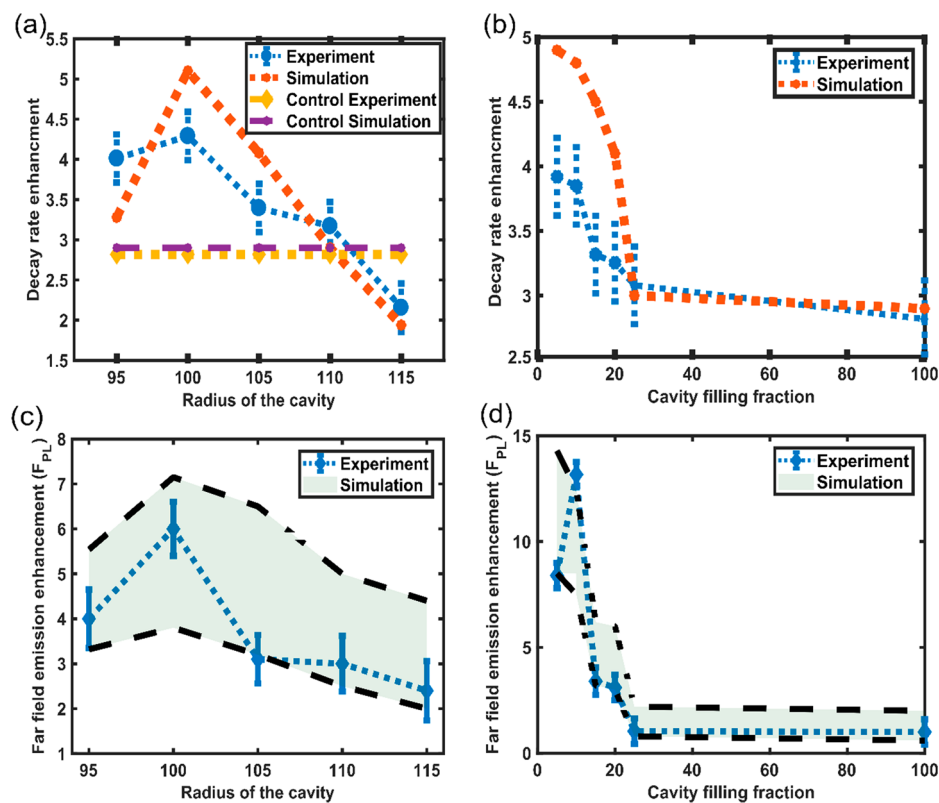


Figure 7. Measured (blue circles) and simulated (red dots) decay rates for a QD coupled to a cavity, normalized to the decay rate of the QD on glass, for (a) cavities with 20% filling fraction and varying radius and (b) 105 nm cavity with different filling fractions. (c and d) Measured (blue dotted) and simulated (shaded region) far-field emission enhancement (F_{PL}) for cavities with different sizes (c) and cavities with a different filling fractions (d), respectively.

monolayer of QDs coupled to HMM cavities. Figure 6(a) shows the time-resolved measurements for three different cavity radii: 95, 105, and 115 nm, respectively. To better understand the variation in decay rate with respect to the cavity size, we have also plotted the decay curves of the QD monolayer placed on top of the bare glass substrate and the bulk reference hyperbolic metamaterial (control sample) in all the figures. From Figure 6(a) it is clear that the decay rate is changing with cavity dimensions, and proper design allows us to increase the decay rate and therefore enhance the emission. It is worth noting that the combination of measurements we have performed (spectral PL and TRPL) validates that the HMM cavities enhance both the far-field radiation rate and far-field emission enhancement (F_{PL}) as well as the decay rate as compared to the bulk (control) sample.

When the cavity size is increased from 95 nm to 115 nm, the HMM cavity resonance is detuned from the QD emission spectrum. For cavities with a radius of 95–105 nm, the cavity resonance overlaps with the QD PL spectra, and therefore the lifetime is shortened ($\tau_{95} = 4.3$ ns, $\tau_{100} = 4.02$ ns, $\tau_{105} = 5.1$ ns), respectively, with respect to $\tau_{\text{bulk}} = 6.2$ ns) by radiative processes, as is shown in Figure 6(a). In contrast, for the larger cavities with a radius of 115 nm the cavity resonance is detuned from the PL spectrum, and therefore the QD lifetime is longer ($\tau_{115} = 8$ ns) and approaches that of QDs on the glass substrate ($\tau_{\text{glass}} = 17.25$ ns). As can be seen, when the cavity is off-resonance with the PL spectrum, it behaves somewhat between the glass and the control sample. Comparing the decay rates for QDs on the glass substrate with decay rates on the bulk HMM control shows that the control lifetime is

shorter than the glass lifetime. However, bearing in mind our spectral measurements presented in Figure 5, we understand that this enhanced decay is nonradiative, thus emphasizing the importance of the HMM cavities in enhancing the radiative decay rate.

Figure 6(b) shows the decay rates of QDs on cavity arrays with three different filling fractions: 5%, 15%, and 25%. The 5% filling fraction array has the fastest decay rate. As the filling fraction increases, the decay rates reach that of the bulk HMM control sample ($\tau_{5\%} = 4.4$ ns, $\tau_{15\%} = 5.2$ ns, $\tau_{25\%} = 5.6$ ns). Decay curves of other sizes and filling fractions of cavities, alongside details regarding decay curve fitting, and corresponding time constants are given in the Supporting Information.

Figure 7 compares the measured far-field emission enhancement and lifetime shortening to FDTD-simulated values. Figure 7(a) shows the experimentally measured enhanced decay rates (TRPL, blue), alongside the FDTD calculated decay rate enhancement (red) of HMM cavity arrays with a constant filling fraction of 20% and a varying cavity radius. These measurements were done in reflection (as described in the Methods section). All results were normalized to the bare glass sample, and they all show enhancement relative to bulk HMM. We observed a clear variation of the normalized decay rate as a function of cavity size with the maximal enhancement observed for cavities with a radius of 100 nm. This is due to the large spectral overlap between the quantum dots' PL emission spectrum and the cavity resonant mode. As the cavity radius reaches 115 nm, the spectral overlap is reduced significantly, and the decay rate becomes closer to the glass decay rate. The decay rate of the control sample is also added in the figure. The

decay rate of the control sample is similar in value to a 110 nm cavity radius and larger than the 115 nm cavity radius due to the broadband Purcell factor. This is because the 115 nm radius cavity has a sharp resonance that is spectrally detuned from the QDs' PL emission peak.

The experimentally measured (blue) and FDTD-calculated emission rate enhancement (red) are in good agreement with each other.

The simulated emission rate enhancement was calculated using the phenomenological theory of quantum emitters coupled to a single metal nanoantenna. This is justified due to the relatively narrow resonance bandwidth of our HMM cavities.^{63,64} Details regarding the emission rate enhancement calculations using FDTD simulations are given in the Supporting Information.⁶⁵

Figure 7(b) shows the experimentally measured enhanced decay rates (TRPL, blue), alongside the FDTD-calculated decay rate enhancement (red) as a function of area fraction for cavities with a constant radius of 105 nm. All results were normalized to the bare glass sample. With the increase in filling fraction, the decay rate decreases (and lifetime increases), and at a filling fraction of 25% the emission rate goes down nearly to that of the control sample, which is indicated as 100% filling fraction in Figure 7(b). This behavior is also nicely predicted by our FDTD simulation (red).

Figure 7(c) compares the measured far-field emission enhancement ($FPL(\text{exp}) = IPL(\text{HMM})/IPL(\text{glass})$) to the FDTD-calculated far-field emission enhancement ($FPL(\text{sim})$) (shaded region) of HMM cavity arrays with a constant filling fraction of 20% and a varying cavity radius. The far-field emission enhancement (Figure 7(c)) shows a similar variation trend of decay rate enhancement (Figure 7(a)), albeit with different values, mostly due to the ohmic loss. This indicates that the steady-state far-field emission enhancement is related to the radiative rate enhancement by the HMM cavity. However, based on the larger enhancement of steady-state PL (compared with decay rate), we claim that a major contribution to this enhancement is the HMM cavity acting as an antenna, coupling dipole fields to radiation. The experimental far-field emission is within the FDTD simulation limit. The reason for the uncertainty in the simulation (denoted by the shaded region) is the uncertainty in the internal quantum efficiency " η " of the QDs. In our simulations we have taken the values of " η " to be bounded between 0.2 and 0.5, which corresponds to the two limits defining the shaded region of the FDTD simulations. The details of the FDTD simulations are given in the Supporting Information. Figure 7(d) compares the far-field emission enhancement measured from the HMM cavity array ($FPL(\text{exp}) = IPL(\text{HMM})/IPL(\text{glass})$) to the one calculated by FDTD (shaded region) for different filling fractions and assuming a constant cavity radius of 105 nm.

As can be seen, the PL enhancement shows a nonmonotonic variation as a function of the filling fraction. The PL emission enhancement is large at filling fractions of both 5% and 10%, even when compared to QDs on the bare glass substrate.

The reported variation of emission rates and PL intensities is interpreted as follows: for a filling fraction of 5%, the observed enhancement in PL is small (~ 1.5). This can be explained by the relatively low cavity Q -factor (~ 4 , see Figure 3 and Supporting Information), providing low enhancement even though the ohmic loss is also expected to be low due to the small metal fraction. As the filling fraction increases to 10%, the

array becomes denser (*i.e.*, higher ohmic loss is expected); however the quality factor increases (~ 25), which results in great enhancement of both PL and radiation rate. By further increasing the filling fractions beyond 15%, the ohmic loss becomes dominant, and a slight increase in Q -factor beyond 25 cannot compensate for radiation absorption in the cavities. It is thus very likely that the large metal portion results in quenching, indicated by the radiative rates being faster and approaching that of bulk HMM, along with the reduction in PL. The FDTD simulation region (shaded region in Figure 7(d)) is in good agreement with the experimental results.

It is worth noting that the Q -factors are on the order of ~ 20 – 25 , which is reasonable for metallic lossy cavities, but still very low compared to the dielectric cavities. A useful figure of merit for light–matter interactions around nanocavities is Q/V_m , which for our case, with the ultrasmall mode volumes of these cavities ($V_m \approx 5 \times 10^{-5} (\lambda_0)^3$), results in Q/V_m values of *ca.* 5×10^5 , which is a reasonable value for enhanced light–matter interactions. Even though nonradiative metallic losses are the major bottleneck in using metal-based plasmonic and metamaterial structures for enhancing light emission, our work shows promising applications of light–matter interactions in ultrasmall mode volume hyperbolic nanocavities. It is worth mentioning other approaches for loss mitigation, such as loss compensation with gain medium^{66–68} and low-temperature operation.⁶⁹

In conclusion, our work on enhancing light–matter interactions using ultrasmall mode volume nanocavities with large (Q/V_m) values demonstrates applications of these cavities from cavity quantum electrodynamics to nonlinear optics and biosensors.

CONCLUSIONS

In this article, we report the design and fabrication of HMM cavities, and we demonstrate their ability to enhance the far-field emission of quantum emitters in the visible regime. We show that the emission enhancement is a result of increasing the LDOS for radiative processes (shown by lifetime measurements) combined with supreme coupling to radiation (shown by steady-state PL measurements), both achieved by coupling the QDs to our HMM cavities. By this, we show that for true emission enhancement an increase in LDOS (or Purcell effect) alone is insufficient, as this may lead to nonradiative decays, and that the far-field coupling is invaluable for such applications. We demonstrate the abilities of HMM cavities as a completely artificial and engineered material and for multiple applications in fields of photonics and quantum optics. Coupling to quantum dots in the visible frequency and free-space radiative emission enhancement of HMM cavities for future applications in the enhancement of solid-state light-emitting devices were demonstrated. We also showed the modulation of emission enhancement as isofrequency topology of the HMM cavities. We believe this work demonstrates using ultrasmall mode volume HMM cavities for applications ranging from nanophotonic devices to cavity-enhanced nanobiosensors.

METHODS

Sample Fabrication. All the samples were fabricated on top of glass substrates.⁷⁰ First, a 200 nm thick poly(methyl methacrylate) (PMMA) 950 K e-beam resist from Microchem was spin-coated over the substrate. To avoid charging, we have used a conducting water-soluble layer (E-spacer) on top of the PMMA layer. Then, the

sample was patterned using a Raith Eline electron beam system with a 20 kV acceleration voltage, ~ 10 mm working distance, $10\ \mu\text{m}$ aperture size, and an optimized dose of $500\ \frac{\mu\text{C}}{\text{cm}^2}$ for patterning an area of $200\ \mu\text{m} \times 200\ \mu\text{m}$ for each cavity array. The exposed PMMA was developed for 60 s using a MIBK/IPA (1:3) solution. Six alternating layers consisting of Al_2O_3 (24 nm, three layers) and Ag (16 nm, three layers), followed by a 5 nm thick Al_2O_3 spacer layer on top, were evaporated on top of the substrate using an e-beam evaporator at deposition rates of 0.3 and 0.5 $\text{\AA}/\text{s}$, respectively. Lift-off was used to obtain the designed structure by treating the sample with acetone using an ultrasonic bath for 5 min.

Transmission Measurement. Following the design and fabrication of the HMM cavities, we have experimentally characterized their optical response. Transmission measurements were done by illuminating the sample with a white light source (tungsten-halogen lamp) through a microscope condenser lens.⁷¹ The transmitted light is collected by an objective lens (Nikon, 50 \times , NA 0.45) and directed into one of the following two spectrometers, depending upon the wavelength of interest: Ocean Optics, Flame, for the visible regime and Horiba, microHR, for the NIR regime.⁷¹ Both spectrograph measurements were normalized to the transmission through the system and combined to create an optical response of the entire frequency range. The individual spectra from each spectrograph and their normalization are shown in the [Supporting Information](#).

PL Measurements. For both steady-state and TRPL measurements CdSe/ZnS core-shell quantum dots with an average radius around 6 nm purchased from MKNano (Canada) were used without further purification. The average concentration is about 10 mg/mL of QD colloidal solution in toluene. This QD solution in toluene is spin coated on the HMM cavity array at 1500 rpm for 60 s to form a uniform monolayer with excellent coverage area. The PL peak of the QDs in solution is around 630 nm, which matches with the PL spectrum of QDs spin-coated films on the glass substrate. Both steady-state and time-resolved measurements were performed using an inverted microscope in reflection mode. For the steady-state measurements the sample is excited using a supercontinuum laser (rep. rate 80 MHz) filtered to a spectral width of ~ 4 nm around a central wavelength of 514 nm. PL emission is separated by a dichroic mirror and a long-pass filter, both with cutoff wavelengths of 550 nm. In the case of time-resolved measurements, the same excitation and collection setup was used except for the source repetition rate, which was lowered to 20 MHz. The PL signal was coupled to a fiber that is connected to either the spectrograph (in the case of steady-state measurements) or to a single photon detector (SPAD, for time-resolved measurement).

Numerical Simulations. FDTD simulations were performed using commercial software (FDTD Solutions, Lumerical Inc.). All the simulations were performed with a mesh size of 2 nm. For the far-field radiation enhancement simulation, a dipole source was used with an emission spectrum that matches the QD emission spectrum. By varying the dipole position and polarization we have calculated the average enhancement of decay rates for the given system. More details about simulations are given in the [Supporting Information](#).

ASSOCIATED CONTENT

Supporting Information

The Supporting Information is available free of charge on the ACS Publications website at DOI: [10.1021/acsnano.9b05730](https://doi.org/10.1021/acsnano.9b05730).

Figures of all the transmission data for different cavity arrays; details of FDTD simulations containing the electric field distribution of cavity modes, calculating the total decay rate and the far-field emission enhancement including the effects of dipole polarization and distance, radiative and nonradiative decay rates; time-resolved photoluminescence data and fitting parameters. (PDF)

AUTHOR INFORMATION

Corresponding Author

*E-mail: ulevy@mail.huji.ac.il

ORCID

S. R. K. Chaitanya Indukuri: [0000-0003-3956-6151](https://orcid.org/0000-0003-3956-6151)

Jonathan Bar-David: [0000-0002-4464-636X](https://orcid.org/0000-0002-4464-636X)

Uriel Levy: [0000-0002-5918-1876](https://orcid.org/0000-0002-5918-1876)

Author Contributions

*S. R. K. C. Indukuri and J. Bar-David contributed equally.

Notes

The authors declare no competing financial interest.

ACKNOWLEDGMENTS

We acknowledge funding from the Israeli Ministry of Science and Technology and The Air Force Office of Scientific Research. J.B.D. acknowledges the support of the applied research scholarship of the Israeli Ministry of Science and Technology.

REFERENCES

- (1) Gérard, J. M.; Sermage, B.; Gayral, B.; Legrand, B.; Costard, E.; Thierry-Mieg, V. Enhanced Spontaneous Emission by Quantum Boxes in a Monolithic Optical Microcavity. *Phys. Rev. Lett.* **1998**, *81*, 1110–1113.
- (2) Reithmaier, J. P.; Sek, G.; Löffler, A.; Hofmann, C.; Kuhn, S.; Reitzenstein, S.; Keldysh, L. V.; Kulakovskii, V. D.; Reinecke, T. L.; Forchel, A. Strong Coupling in a Single Quantum Dot-Semiconductor Microcavity System. *Nature* **2004**, *432*, 197–200.
- (3) Yoshle, T.; Scherer, A.; Hendrickson, J.; Khitrova, G.; Gibbs, H. M.; Rupper, G.; Ell, C.; Shchekin, O. B.; Deppe, D. G. Vacuum Rabi Splitting with a Single Quantum Dot in a Photonic Crystal Nanocavity. *Nature* **2004**, *432*, 200–203.
- (4) Lodahl, P.; Van Driel, A. F.; Nikolaev, I. S.; Irman, A.; Overgaag, K.; Vanmaekelbergh, D.; Vos, W. L. Controlling the Dynamics of Spontaneous Emission from Quantum Dots by Photonic Crystals. *Nature* **2004**, *430*, 654–657.
- (5) Gjerding, M. N.; Petersen, R.; Pedersen, T. G.; Mortensen, N. A.; Thygesen, K. S. Layered van Der Waals Crystals with Hyperbolic Light Dispersion. *Nat. Commun.* **2017**, *8*, 320.
- (6) Armani, D. K.; Kippenberg, T. J.; Spillane, S. M.; Vahala, K. J. Ultra-High-Q Toroid Microcavity on a Chip. *Nature* **2003**, *421*, 925–928.
- (7) Artemyev, M. V.; Woggon, U.; Wannemacher, R.; Jaschinski, H.; Langbein, W. Light Trapped in a Photonic Dot: Microspheres Act as a Cavity for Quantum Dot Emission. *Nano Lett.* **2001**, *1*, 309–314.
- (8) Akahane, Y.; Asano, T.; Song, B. S.; Noda, S. High-Q Photonic Nanocavity in a Two-Dimensional Photonic Crystal. *Nature* **2003**, *425*, 944–947.
- (9) Ogawa, S.; Imada, M.; Yoshimoto, S.; Makoto Okano, S. N. Control of Light Emission by 3D Photonic Crystals. *Science* **2004**, *305*, 227–230.
- (10) Ilchenko, V. S.; Savchenkov, A. A.; Matsko, A. B.; Maleki, L. Nonlinear Optics and Crystalline Whispering Gallery Mode Cavities. *Phys. Rev. Lett.* **2004**, *92*, 043903.
- (11) Eichenfield, M.; Camacho, R.; Chan, J.; Vahala, K. J.; Painter, O. A Picogram- and Nanometre-Scale Photonic-Crystal Optomechanical Cavity. *Nature* **2009**, *459*, 550–555.
- (12) Hennessy, K.; Badolato, A.; Winger, M.; Gerace, D.; Atature, M.; Gulde, S.; Falt, S.; Hu, E. L.; Imamoglu, A. Quantum Nature of a Strongly Coupled Single Quantum Dot-Cavity System. *Nature* **2007**, *445*, 896–899.
- (13) Visio, M. Sub-Wavelength Optics. *Nature* **2003**, *10*, 63–73.
- (14) Zayats, A. V.; Smolyaninov, I. I.; Maradudin, A. A. Nano-Optics of Surface Plasmon Polaritons. *Phys. Rep.* **2005**, *408*, 131–314.

- (15) Seo, M.; Kwon, S.; Ee, H.; Park, H. Full Three-Dimensional Subwavelength High-Q Surface-Plasmon-Polariton Cavity. *Nano Lett.* **2009**, *9*, 4078–4082.
- (16) Min, B.; Ostby, E.; Sorger, V.; Ulin-Avila, E.; Yang, L.; Zhang, X.; Vahala, K. High-Q Surface-Plasmon-Polariton Whispering-Gallery Microcavity. *Nature* **2009**, *457*, 455–458.
- (17) Tserkezis, C.; Esteban, R.; Sigle, D. O.; Mertens, J.; Herrmann, L. O.; Baumberg, J. J.; Aizpurua, J. Hybridization of Plasmonic Antenna and Cavity Modes: Extreme Optics of Nanoparticle-on-Mirror Nanogaps. *Phys. Rev. A: At., Mol., Opt. Phys.* **2015**, *92*, 053811.
- (18) Akselrod, G. M.; Argyropoulos, C.; Hoang, T. B.; Ciraci, C.; Fang, C.; Huang, J.; Smith, D. R.; Mikkelsen, M. H. Probing the Mechanisms of Large Purcell Enhancement in Plasmonic Nanoantennas. *Nat. Photonics* **2014**, *8*, 835–840.
- (19) Hoang, T. B.; Akselrod, G. M.; Argyropoulos, C.; Huang, J.; Smith, D. R.; Mikkelsen, M. H. Ultrafast Spontaneous Emission Source Using Plasmonic Nanoantennas. *Nat. Commun.* **2015**, *6*, 1–7.
- (20) Zhou, W.; Dridi, M.; Suh, J. Y.; Kim, C. H.; Co, D. T.; Wasielewski, M. R.; Schatz, G. C.; Odom, T. W. Lasing Action in Strongly Coupled Plasmonic Nanocavity Arrays. *Nat. Nanotechnol.* **2013**, *8*, 506–511.
- (21) Chikkaraddy, R.; De Nijs, B.; Benz, F.; Barrow, S. J.; Scherman, O. A.; Rosta, E.; Demetriadou, A.; Fox, P.; Hess, O.; Baumberg, J. J. Single-Molecule Strong Coupling at Room Temperature in Plasmonic Nanocavities. *Nature* **2016**, *535*, 127–130.
- (22) Smith, D. R.; Smith, D. R.; Pendry, J. B.; Wiltshire, M. C. K. Metamaterials and Negative Refractive Index. *Science* **2009**, *788*, 788–793.
- (23) Shelby, R. A.; Smith, D. R.; Schultz, S. Experimental Verification of a Negative Index of Refraction. *Science* **2001**, *292*, 77–79.
- (24) Liu, Z.; Lee, H.; Xiong, Y.; Sun, C.; Zhang, X. Far-Field Optical Hyperlens Magnifying Sub-Diffraction-Limited Objects. *Science* **2007**, *315*, 1686.
- (25) Shalin, A. S.; Ginzburg, P.; Orlov, A. A.; Iorsh, I.; Belov, P. A.; Kivshar, Y. S.; Zayats, A. V. Optical Cloaking with ENZ-Metamaterials. *2015 9th Int. Congr. Adv. Electromagn. Mater. Microwaves Opt. Metamaterials*; 2015, Vol. 1, pp 487–489.
- (26) Ergin, T.; Stenger, N.; Brenner, P.; Pendry, J. B.; Wegener, M. Three-Dimensional Invisibility Cloak at Optical Wavelengths. *Science* **2010**, *328*, 337–340.
- (27) Choi, M.; Lee, S. H.; Kim, Y.; Kang, S. B.; Shin, J.; Kwak, M. H.; Kang, K.-Y.; Lee, Y.-H.; Park, N.; Min, B. A Terahertz Metamaterial with Unnaturally High Refractive Index. *Nature* **2011**, *470*, 369–373.
- (28) Ginzburg, P.; Roth, D. J.; Nasir, M. E.; Segovia, P.; Alexey, V.; James Levitt, K.; Hirvonen, L. M.; Wells, B.; Klaus, S.; Richards, D.; Viktor, A.; Podolskiy, A. V. Z. Spontaneous Emission in Non-Local Materials. *Light: Sci. Appl.* **2017**, *6*, e16273.
- (29) Poddubny, A.; Iorsh, I.; Belov, P.; Kivshar, Y. Hyperbolic Metamaterials. *Nat. Photonics* **2013**, *7*, 948–957.
- (30) Krishnamoorthy, H. N. S.; Jacob, Z.; Narimanov, E.; Kretzschmar, I.; Menon, V. M. Topological Transitions in Metamaterials. *Science* **2012**, *336*, 205–209.
- (31) Cortes, C. L.; Newman, W.; Molesky, S.; Jacob, Z. Quantum Nanophotonics Using Hyperbolic Metamaterials. *J. Opt.* **2012**, *14*, 063001.
- (32) Indukuri, C.; Yadav, R. K.; Basu, J. K. Broadband Room Temperature Strong Coupling between Quantum Dots and Metamaterials. *Nanoscale* **2017**, *9*, 11418–11423.
- (33) Tong, L.; Pakizeh, T.; Feuz, L.; Dmitriev, A. Highly Directional Bottom-Up 3D Nanoantenna for Visible Light. *Sci. Rep.* **2013**, *3*, 2311.
- (34) Jacob, Z.; Smolyaninov, I. I.; Narimanov, E. E. Broadband Purcell Effect: Radiative Decay Engineering with Metamaterials. *Appl. Phys. Lett.* **2012**, *100*, 181105.
- (35) Jacob, Z.; Kim, J. Y.; Naik, G. V.; Boltasseva, A.; Narimanov, E. E.; Shalaev, V. M. Engineering Photonic Density of States Using Metamaterials. *Appl. Phys. B: Lasers Opt.* **2010**, *100*, 215–218.
- (36) Tumkur, T.; Zhu, G.; Black, P.; Barnakov, Y. A.; Bonner, C. E.; Noginov, M. A. Control of Spontaneous Emission in a Volume of Functionalized Hyperbolic Metamaterial. *Appl. Phys. Lett.* **2011**, *99*, 2009–2012.
- (37) Poddubny, A. N.; Belov, P. A.; Ginzburg, P.; Zayats, A. V.; Kivshar, Y. S. Microscopic Model of Purcell Enhancement in Hyperbolic Metamaterials. *Phys. Rev. B: Condens. Matter Mater. Phys.* **2012**, *86*, 035148.
- (38) Poddubny, A. N.; Belov, P. A.; Kivshar, Y. S. Spontaneous Radiation of a Finite-Size Dipole Emitter in Hyperbolic Media. *Phys. Rev. A: At., Mol., Opt. Phys.* **2011**, *84*, 023807.
- (39) Urbas, A. M.; Jacob, Z.; Negro, L. D.; Engheta, N.; Boardman, A. D.; Egan, P.; Khanikaev, A. B.; Menon, V.; Ferrera, M.; Kinsey, N.; DeVault, C.; Kim, J.; Shalaev, V.; Boltasseva, A.; Valentine, J.; Pfeiffer, C.; Grbic, A.; Narimanov, E.; Zhu, L.; Nealey, P. F.; et al. Roadmap on Optical Metamaterials. *J. Opt.* **2016**, *18*, 093005.
- (40) Guo, Y.; Newman, W.; Cortes, C. L.; Jacob, Z. Applications of Hyperbolic Metamaterial Substrates. *Adv. Optoelectron.* **2012**, *2012*, 1–10.
- (41) Galfsky, T.; Krishnamoorthy, H. N. S.; Newman, W.; Narimanov, E. E.; Jacob, Z.; Menon, V. M. Active Hyperbolic Metamaterials: Enhanced Spontaneous Emission and Light Extraction. *Optica* **2015**, *2*, 62–65.
- (42) Shen, K.; Ku, C.; Hsieh, C.; Kuo, H.; Cheng, Y. Deep-Ultraviolet Hyperbolic Metacavity Laser. *Adv. Mater.* **2018**, *30*, 1706918.
- (43) Li, L.; Wang, W.; Luk, T. S.; Yang, X.; Gao, J. Enhanced Quantum Dot Spontaneous Emission with Multilayer Metamaterial Nanostructures. *ACS Photonics* **2017**, *4*, 501–508.
- (44) Lu, D.; Kan, J. J.; Fullerton, E. E.; Liu, Z. Enhancing Spontaneous Emission Rates of Molecules Using Nanopatterned Multilayer Hyperbolic Metamaterials. *Nat. Nanotechnol.* **2014**, *9*, 48–53.
- (45) Yao, J.; Yang, X.; Yin, X.; Bartal, G.; Zhang, X. Three-Dimensional Nanometer-Scale Optical Cavities of Indefinite Medium. *Proc. Natl. Acad. Sci. U. S. A.* **2011**, *108*, 11327–11331.
- (46) Yang, X.; Yao, J.; Rho, J.; Yin, X.; Zhang, X. Experimental Realization of Three-Dimensional Indefinite Cavities at the Nanoscale with Anomalous Scaling Laws. *Nat. Photonics* **2012**, *6*, 450–454.
- (47) Guclu, C.; Luk, T. S.; Wang, G. T.; Capolino, F. Radiative Emission Enhancement Using Nano-Antennas Made of Hyperbolic Metamaterial Resonators. *Appl. Phys. Lett.* **2014**, *105*, 123101.
- (48) Slobozhanyuk, A. P.; Ginzburg, P.; Powell, D. A.; Iorsh, I.; Shalin, A. S.; Segovia, P.; Krasavin, A. V.; Wurtz, G. A.; Podolskiy, V. A.; Belov, P. A.; Zayats, A. V. Purcell Effect in Hyperbolic Metamaterial Resonators. *Phys. Rev. B: Condens. Matter Mater. Phys.* **2015**, *92*, 195127.
- (49) Shekhar, P.; Atkinson, J.; Jacob, Z. Hyperbolic Metamaterials: Fundamentals and Applications. *Nano Converg* **2014**, *1*, 1–14.
- (50) Kaina, N.; Lemoult, F.; Fink, M.; Lerosey, G. Ultra Small Mode Volume Defect Cavities in Spatially Ordered and Disordered Metamaterials. *Appl. Phys. Lett.* **2013**, *102*, 144104.
- (51) Maccaferri, N.; Zhao, Y.; Isoniemi, T.; Iarossi, M.; Parracino, A.; Strangi, G.; De Angelis, F. Hyperbolic Meta-Antennas Enable Full Control of Scattering and Absorption of Light. *Nano Lett.* **2019**, *19*, 1851–1859.
- (52) Maccaferri, N.; Bergamini, L.; Pancaldi, M.; Schmidt, M. K.; Kataja, M.; van Dijken, S.; Zabala, N.; Aizpurua, J.; Vavassori, P. Anisotropic Nanoantenna-Based Magnetoplasmonic Crystals for Highly Enhanced and Tunable Magneto-Optical Activity. *Nano Lett.* **2016**, *16*, 2533–2542.
- (53) Peragut, F.; Cerruti, L.; Baranov, A.; Hugonin, J. P.; Taliercio, T.; De Wilde, Y.; Greffet, J. J. Hyperbolic Metamaterials and Surface Plasmon Polaritons. *Optica* **2017**, *4*, 1409–1415.
- (54) Luk, T. S.; Kim, I.; Campione, S.; Howell, S. W.; Subramania, G. S.; Grubbs, R. K.; Brener, I.; Chen, H.-T.; Fan, S.; Sinclair, M. B. Near-Infrared Surface Plasmon Polariton Dispersion Control with Hyperbolic Metamaterials. *Opt. Express* **2013**, *21*, 11107–11114.

(55) Celebrano, M.; Wu, X.; Baselli, M.; Großmann, S.; Biagioni, P.; Locatelli, A.; De Angelis, C.; Cerullo, G.; Osellame, R.; Hecht, B.; Duò, L.; Ciccacci, F.; Finazzi, M. Mode Matching in Multiresonant Plasmonic Nanoantennas for Enhanced Second Harmonic Generation. *Nat. Nanotechnol.* **2015**, *10*, 412–417.

(56) Tuccio, S.; Razzari, L.; Alabastri, A.; Toma, A.; Liberale, C.; De Angelis, F.; Candeloro, P.; Das, G.; Giugni, A.; Fabrizio, E. Di; Zaccaria, R. P. Direct Determination of the Resonance Properties of Metallic Conical Nanoantennas. *Opt. Lett.* **2014**, *39*, 571–573.

(57) Zhukovsky, S. V.; Kidwai, O.; Sipe, J. E. Physical Nature of Volume Plasmon Polaritons in Hyperbolic Metamaterials. *Opt. Express* **2013**, *21*, 14982–149827.

(58) Zhang, X. M.; Xiao, J. J.; Zhang, Q.; Li, L. M.; Yao, Y. Plasmonic TM-Like Cavity Modes and the Hybridization in Multilayer Metal-Dielectric Nanoantenna. *Opt. Express* **2015**, *23*, 16122–16132.

(59) Lou, F.; Yan, M.; Thylen, L.; Qiu, M.; Wosinski, L. Whispering Gallery Mode Nanodisk Resonator Based on Layered Metal-Dielectric Waveguide. *Opt. Express* **2014**, *22*, 8490–8502.

(60) Ginzburg, P. Cavity Quantum Electrodynamics in Application to Plasmonics and Metamaterials. *Rev. Phys.* **2016**, *1*, 120–139.

(61) Valagiannopoulos, C. A.; Mirmoosa, M. S.; Nefedov, I. S.; Tret'yakov, S. A.; Simovski, C. R. Hyperbolic-Metamaterial Antennas for Broadband Enhancement of Dipole Emission to Free Space. *J. Appl. Phys.* **2014**, *116*, 163106.

(62) Tanaka, K.; Plum, E.; Ou, J. Y.; Uchino, T.; Zheludev, N. I. Multifold Enhancement of Quantum Dot Luminescence in Plasmonic Metamaterials. *Phys. Rev. Lett.* **2010**, *105*, 227403.

(63) Anger, P.; Bharadwaj, P.; Novotny, L. Enhancement and Quenching of Single-Molecule Fluorescence. *Phys. Rev. Lett.* **2006**, *96*, 113002.

(64) Kühn, S.; Håkanson, U.; Rogobete, L.; Sandoghdar, V. Enhancement of Single-Molecule Fluorescence Using a Gold Nanoparticle as an Optical Nanoantenna. *Phys. Rev. Lett.* **2006**, *97*, 017402.

(65) Indukuri, C.; Mukherjee, A.; Basu, J. K. Tailoring Local Density of Optical States to Control Emission Intensity and Anisotropy of Quantum Dots in Hybrid Photonic-Plasmonic Templates. *Appl. Phys. Lett.* **2015**, *106*, 1311111.

(66) De Leon, I.; Berini, P. Amplification of Long-Range Surface Plasmons by a Dipolar Gain Medium. *Nat. Photonics* **2010**, *4*, 382–387.

(67) García-blanco, S. M.; Pollnau, M.; Bozhevolnyi, S. I. Loss Compensation in Long-Range Dielectric-Loaded Surface Plasmon-Polariton Waveguides. *Opt. Express* **2011**, *19*, 25298–25310.

(68) Nezhad, M.; Tetz, K.; Fainman, Y. Gain Assisted Propagation of Surface Plasmon Polaritons on Planar Metallic Waveguides. *Opt. Express* **2004**, *12*, 4072–4079.

(69) Bouillard, J. S. G.; Dickson, W.; O'Connor, D. P.; Wurtz, G. A.; Zayats, A. V. Low-Temperature Plasmonics of Metallic Nanostructures. *Nano Lett.* **2012**, *12*, 1561–1565.

(70) Arora, P.; Talker, E.; Mazurski, N.; Levy, U. Dispersion Engineering with Plasmonic Nano Structures for Enhanced Surface Plasmon Resonance Sensing. *Sci. Rep.* **2018**, *8*, 1–9.

(71) Bar-David, J.; Mazurski, N.; Levy, U. In Situ Planarization of Huygens Metasurfaces by Nanoscale Local Oxidation of Silicon. *ACS Photonics* **2017**, *4*, 2359–2366.